RSC Advances

ROYAL SOCIETY OF CHEMISTRY

PAPER

View Article Online
View Journal | View Issue

Check for updates

Cite this: *RSC Adv.*, 2024, **14**, 23672

High precision deep-learning model combined with high-throughput screening to discover fused [5,5] biheterocyclic energetic materials with excellent comprehensive properties†

Youhai Liu,[a] Fusheng Yang, *[a] Wenquan Zhang, *[b] Honglei Xia,[b] Zhen Wu[a] and Zaoxiao Zhang[a]

Received 1st May 2024
Accepted 16th July 2024

DOI: 10.1039/d4ra03233k

rsc.li/rsc-advances

Finding novel energetic materials with good comprehensive performance has always been challenging because of the low efficiency in conventional trial and error experimental procedure. In this paper, we established a deep learning model with high prediction accuracy using embedded features in Directed Message Passing Neural Networks. The model combined with high-throughput screening was shown to facilitate rapid discovery of fused [5,5] biheterocyclic energetic materials with high energy and excellent thermal stability. Density Functional Theory (DFT) calculations proved that the performances of the targeting molecules are consistent with the predicted results from the deep learning model. Furthermore, 6,7-trinitro-3*H*-pyrrolo[1,2-*b*][1,2,4]triazo-5-amine with both good detonation properties and thermal stability was screened out, whose crystal structure and intermolecular interactions were also analyzed.

Introduction

Energetic materials are a type of compound or mixture containing explosive groups or oxidants and fuels, which undergo intense redox reactions under specific external energy stimuli, releasing a large amount of energy. Energetic materials are widely used in weapons and equipment, aerospace propulsion, engineering construction, mineral mining and other fields.[1–5] Energy and stability are the two most important properties of energetic materials. However, a relationship of mutual contradiction is always present between them. Therefore, the development of energetic materials with high energy and outstanding stability simultaneously remains a great challenge. Recently, fused cyclic energetic materials, which feature a unique conjugated structure consisting of shared atoms and bonds, has been considered as a promising alternative to traditional energetic materials.[6] Fused heterocyclic energetic materials exhibit high heat of formation due to their planar fused backbone with multiple nitrogen atoms, meanwhile the presence of π–π interactions between the fused ring endows them with high thermal stability.[7–11] Among fused backbones, [5,5]-fused ring is the simplest one for energetic molecules construction.[12,13] In recent years, several representative structures of fused [5,5]-bicyclic heterocycle energetic materials were designed and synthesized.[13–16] However, these molecules were obtained based on the method of structural design, such as increasing number of N atoms into a fused ring, or substituting explosophoric groups like $-NO_2$, $-NHNO_2$, $-C(NO_2)_2$, $-NH_2$ or $-C(NO_2)_3$ at certain positions, which heavily relies on the chemical experience (intuition) of researchers, develop through trial-and-error processes, involving long period, high costs and safety risks.[17]

In the past decades, with the advent of the big data era, machine learning (ML) technique has been widely used in almost all the material research fields, such as organic photoelectric materials, perovskite materials, lithium-ion battery materials, photovoltaic materials *etc.*[18–22] The application of machine learning methods in energetic materials has also drawn increasing attention. In order to shorten the development cycle of energetic materials, recent work[23–28] presented attempts to use high-throughput screening methods together with ML to target new promising explosives, including insensitive high explosives (IHEs),[23] molten castable explosives,[24] fluorinated explosives,[25] bridged explosive,[27] and some positive results were well achieved. However, mostly traditional machine learning models such as KRR,[29] SVM[30] were used without considering specific characteristics of candidate molecules, resulting in relatively low prediction accuracy for certain crucial properties, *e.g.* decomposition temperature.

---

[a] School of Chemical Engineering and Technology, Xi'an Jiaotong University, Xi'an 710049, China. E-mail: yang.fs@mail.xjtu.edu.cn

[b] Research Center of Energetic Material Genome Science, Institute of Chemical Materials, China Academy of Engineering Physics (CAEP), Mianyang, 621900, P. R. China. E-mail: zhangwq-cn@caep.cn

† Electronic supplementary information (ESI) available. See DOI: https://doi.org/10.1039/d4ra03233k

In this work, we present a deep learning model D-MPNN (Directed Message Passing Neural Networks)[31] of embedded molecular descriptors combined with high-throughput molecular generation, so as to rapidly screen promising target molecules from 2698 generated fused [5,5]-bicyclic heterocycle structures. After the screening procedure, 2,6,7-trinitro-3*H*-pyrrolo[1,2-*b*][1,2,4]triazo-5-amine (ID number:1439), a promising fused [5,5] biheterocyclic backbone-based energetic material was selected. DFT calculation of the properties, along with crystal structure prediction and intermolecular interaction analysis revealed that this new energetic material has outstanding comprehensive properties, including high energy and good thermal stability. These findings demonstrate the great potential of deep learning combining with embedded features in high-performance energetic materials design.

Methods

Workflow

Firstly, the generation of a large number of molecules is implemented and used as search space of fused [5,5] biheterocyclic energetic materials. Subsequently, the high-precision model was obtained by directed Message Passing Neural Networks (D-MPNN) embedded with features, and was used to predict the molecular properties. After that the virtual screening of energetic materials regarding comprehensive performance was carried out. The workflow has been shown in Fig. 1.

The work mainly includes four steps, the first step is the data collection. The second step is the prediction of energetic materials properties. With the collected dataset as input and the embedded features as enhancements to the graph structure features, the so-called module b outputs a model for property prediction. The third step involves searching for the spatial construction of energetic materials. The final step is molecule screening, which filters candidates based on the property prediction model developed in step 2 (including density, detonation performance, and decomposition temperature) and the search space constructed in step 3. Step 4 is further divided into two stages. In the first stage, the deep learning model is used to rapidly screen materials with high density, explosive velocity and decomposition temperature, whereas in the second stage, the DFT calculation is applied to evaluate the performance of the selected molecules, thereby assessing the predictive accuracy of this model. It is also utilized for analysing the molecular structures and intermolecular interaction of the candidate molecules.

Dataset

Our dataset consists of two parts. The first part is derived from the reference Song, S. *et al.*[29] After removing data of substances involving halogens and duplicates, we obtained 562 compounds with data for density, detonation velocity and detonation pressure, and 545 compounds for decomposition temperature (see dataset1 in the ESI†). Additionally, 379 publicly available data records for energetic compounds were extracted from Elton *et al.*[30] by also removing data of substances involving halogens and duplicates. In total, 941 data for density, detonation velocity and detonation pressure, and 545 data for decomposition temperature were obtained for training regression models. The dataset covers various structures that have been used as constitute of energetic materials, *e.g.* aliphatic, aromatic, monocyclic, and polycyclic. Detailed description about the

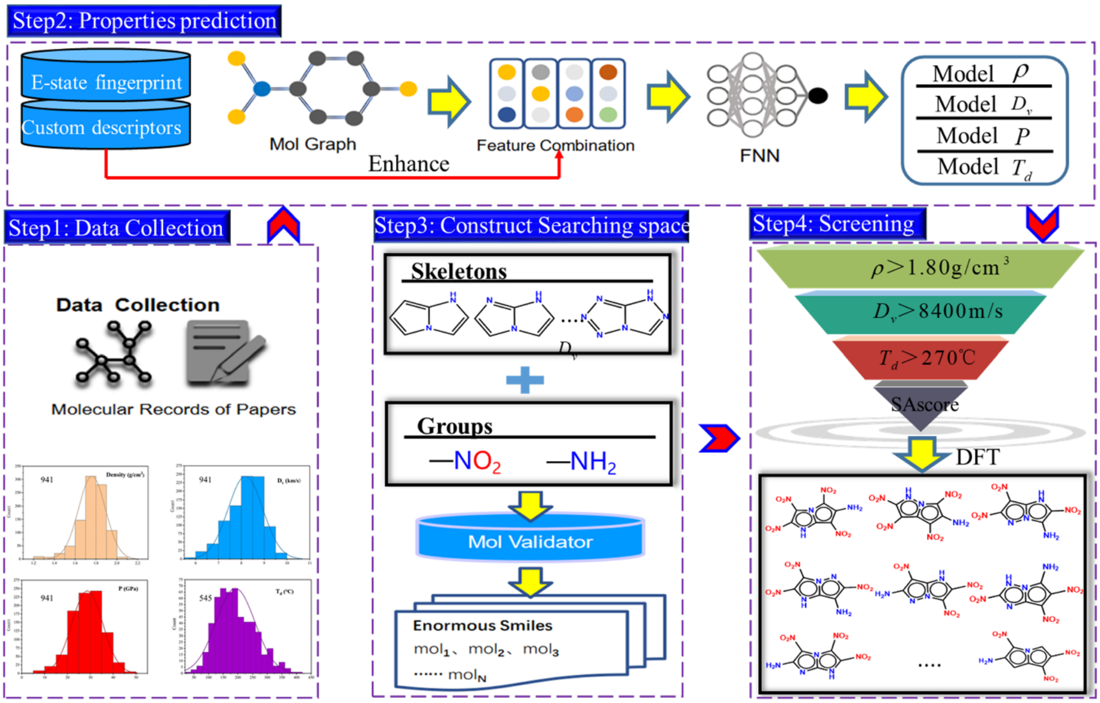

Fig. 1 Workflow of this work.

dataset has been provided in Fig. S1 of the ESI.† Essentially the samples in the dataset are divided into three parts: training set, validation set, and testing set. The training set and validation set are used to train the model and perform fine-turning of hyper-parameters, and the testing set is used for the final verification of the model's generalization performance and accuracy.

D-MPNN

The Message Passing Neural Network (MPNN), that was firstly summarized and proposed by Gilmer *et al.*,[32] is a deep learning model based on graph neural network, operating with atom (node) features and bond (edge) features on an undirected graph G, and has already been used to predict crystal density of energetic materials.[33] Based on this, Yang *et al.*[31] made key adjustments to the original messaging neural network framework by adopting messages related to directed bonds and proposed D-MPNN, which has dramatically reduced the noise caused by nodes passing through random paths. D-MPNN consists of two phases: a message passing phase which constructs neural representations of the molecule by transmitting information through the molecule, and a readout phase which generates the final representation of the molecule to predict the properties of materials.

The message passing is made up of T steps. On each step t, hidden states $h_v^w$and message $m_{vw}{}^t$(v and w represent the nodes between the bond) are updated using message function M_t and vertex update function U_t.

$$m_{vw}{}^{t+1} = \sum_{k\in\{N(v)/w\}} M_t(x_v, x_k, h_{kv}{}^t) \tag{1}$$

$$h_{vw}{}^{t+1} = U_t(h_{vw}{}^t, m_{vw}{}^{t+1}) \tag{2}$$

Where N(v) is the set of adjacent nodes of v in graph G. In the readout phase, the properties are predicted according to the final hidden state through a readout function R:

$$\hat{y} = R(\{h_v T | v \in G\}) \tag{3}$$

Fig. 2 shows the structure and principle of learning molecular expression of D-MPNN neural network. Module in the left-handed panel of the figure, represents the aggregation of information from two directions on the same bond in the molecule and the process of updating and aggregating information, respectively. The internal structure of the feedforward neural network FNN has been displayed in the right-handed panel of the Fig. 2 u represents the encoded feature vector, w represents the weight update in the training process, h represents the hidden layer, and u' is the output of the feature vector, which is passed through the activation function. During the training, the D-MPNN networks use the simplified molecular input line entry specification (SMILES) as the molecular input and predict the outputs value through the loss gradient based on the readout phase.

Embedded molecular descriptors

Ideally, the above-described D-MPNN model described above should be able to extract most information about molecules, which is sufficient to complete specific attribute prediction tasks. Nevertheless, there are still limitations to molecular graph features in practice. Firstly, the decomposition temperature dataset is relatively small in size, with only a few hundred molecules. Due to the limited amount of data, D-MPNN could be not able to recognize and extract all the features related to thermal stability. Secondly, the shapes of molecular graphs are rather irregular, and in the message passing process of MPNN, the number of steps is much fewer than the diameter of the molecular graph. Atoms that are farther apart will never receive information from each other. Therefore, for some properties of energetic materials, there are still considerable number of features that cannot be captured simply *via* the graph convolution process, so it is necessary to add additional features to improve prediction accuracy.

In order to effectively combine the additional features, we modified the readout phase of D-MPNN. The feedforward neural network f can be applied to the cascade of the learned molecular feature vector h and the additional input global feature h_f. The method for model enhancement is also known as

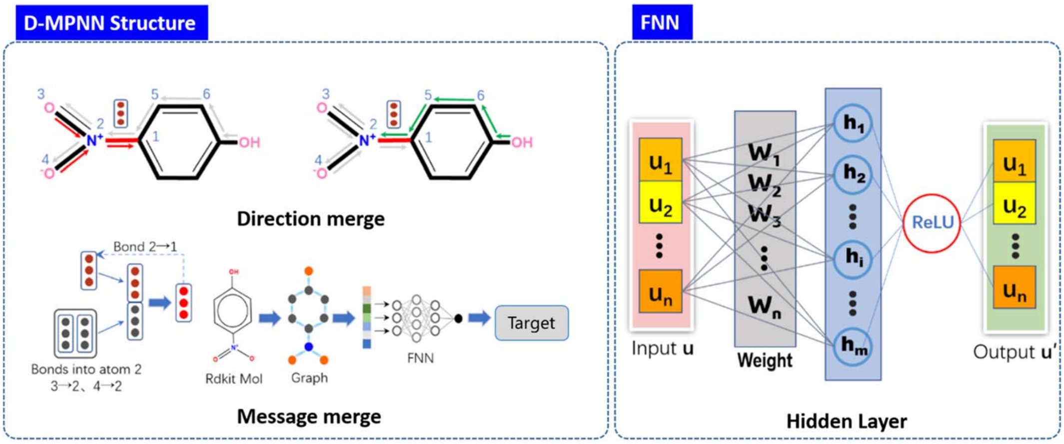

Fig. 2 Structure of D-MPNN neural network.

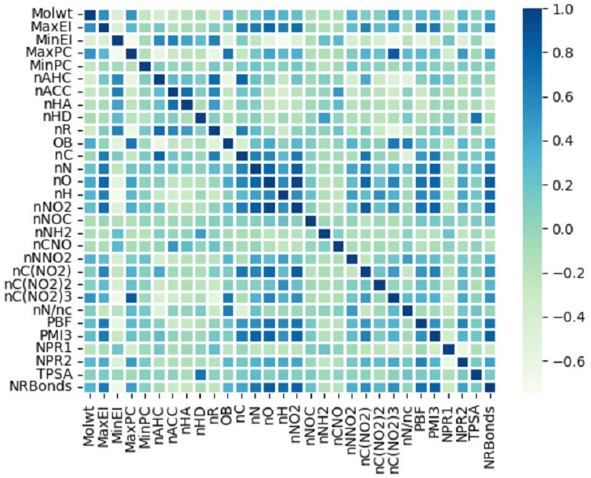

Fig. 3 Custom descriptors set and its heatmap of feature distribution.

knowledge embedding or feature enhancement. The combination of the graph's feature representation h and the global feature h_f can be expressed as the following formula:

$$\hat{y} = f(\mathrm{cat}(h,h_f)) \tag{4}$$

Our embedded molecular features is composed of two parts. The first part includes fingerprints derived from the electrotopological state (E-state) fingerprint, which only involve elements carbon (C), hydrogen (H), oxygen (O), and nitrogen (N) (Table S1 in ESI†), have been widely utilized to construct quantitative relationships between molecular structure and properties.[34,35] The second part includes 30 custom molecular descriptors based on molecular electronic states, the number of typical energy groups, molecular composition and three-dimensional shape of molecules (Table S2 in ESI†) obtained from RDKit library. These custom descriptors enhance the description of molecular composition and shape, such as oxygen balance (OB) and normalized principal distance ratio 1 (NPR1), which will help model learn the properties of energetic materials. The heat map in Fig. 3 demonstrates that most of the custom descriptors are not significantly correlated, which is beneficial for model training.

Molecule generation

We have used a homemade script for generating the molecules. The flow chart of the whole generation process is shown in Fig. 4(a), where the yellow part describes the generation of nitrogen-substituted fused ring using the carbon rings as input and the green part illustrates the process of adding the groups to the mother ring skeleton in a manner of permutation and combination.

Fig. 4(b) shows the generation process of the fused [5,5] biheterocyclic molecules. Initially, the structure of the molecular generation containing six [5,5] bicyclic carbon skeletons, 1*N*-substitution cannot form fused heterocycle structure, therefore we used the structures (from 2*N* to 6*N*) to replace the carbon in the carbon skeleton, by which 112 different fused [5,5] biheterocyclic skeletons were obtained. Collectively, 2698 possible fused [5,5] biheterocyclic were generated *via* the introduction of nitro (used as energetic group)/amino (group used as balance energy and sensitivity) into 112 fused [5,5] biheterocyclic skeletons.

DFT calculation

In this study, we employ density functional theory (DFT) to investigate the key properties of the selected fused [5,5] bicyclic heterocycle energetic materials. The computational calculations were performed using Gaussian 16 (A.03),[36] and the results were analyzed using the wave function analysis software Multiwfn 3.8 (dev),[37] more detail is referred to the ESI.†

Results and discussion

Molecular screening based on predicted properties

We used our dataset to train and test the model of D-MPNN embedded with molecule features comprising of Estate fingerprints and custom descriptors. In general, the framework of D-MPNN can spontaneously generate their features form molecular graphs through message passing and aggregation algorithms to predict the properties. The initial atom and bond features of the model are list in Table S3 and S4.† All features are calculated using the open-source package RDKit.[38] After obtaining hyperparameters *via* Bayesian Optimization.[39] The D-MPNN's depth (number of message-passing steps), hidden size

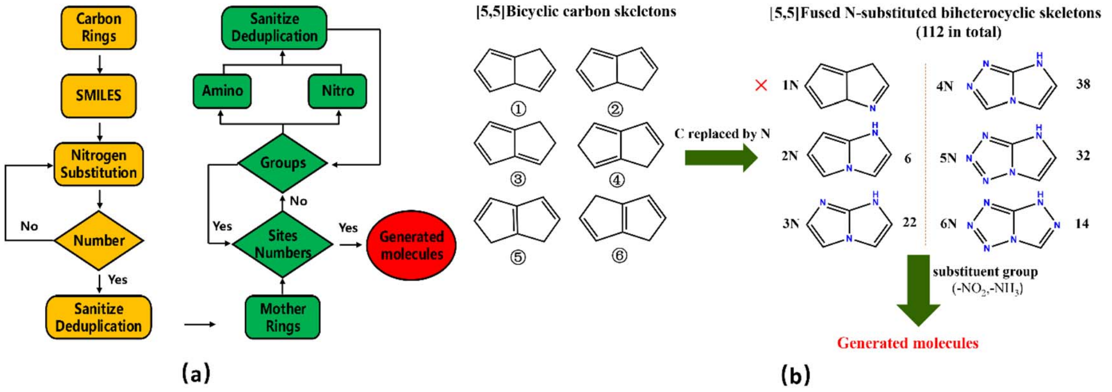

Fig. 4 (a) Flow chart for molecular structural generation; (b) generation process of the fused [5,5] biheterocyclic molecules.

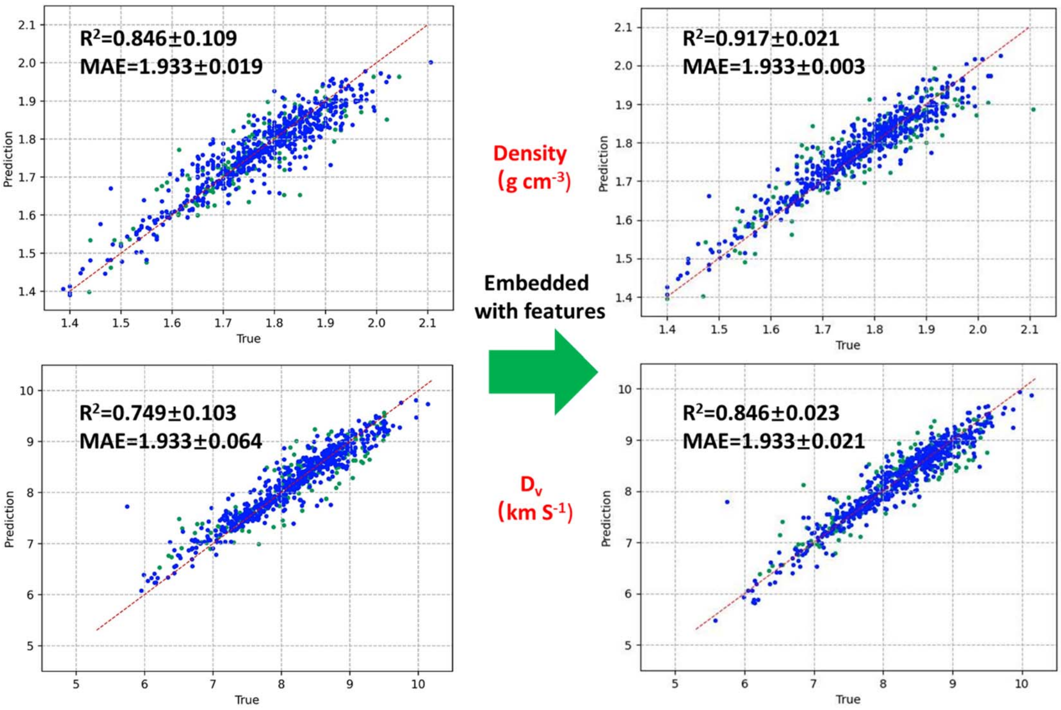

Fig. 5 Prediction results before and after the inclusion of embedded features for density and detonation velocity.

(size of bond message vectors), number of feed-forward network layers, and dropout were set as 5, 1700, 1700, 0.1, respectively. We used a 0.8/0.1/0.1 split for the training, validation, and test sets, and performed 5 folds cross-validation, using ReLU as activation functions, which can extend to act independently on each element of the vector output from the hidden layer, and effectively leverages non-linear activation functions to enhance its capacity for learning and representation of intricate features in the data. Fig. 5 displays the predicted density and detonation velocity before and after the inclusion of embedded features. For density, the R^2 increased from 0.846 to 0.917, while the MAE decreased from 0.0365 to 0.026. The trend is similar for detonation velocity, with R^2 increasing to 0.879 and MAE decreasing to 0.20. This suggests that the predictive accuracy of the model was improved through the incorporation of embedded features. The same effect was also found in the detonation pressure and decomposition temperature (see Fig S3 in ESI†). Such high accuracy may result from the reasonable features added, which can capture both crystal and molecular characteristics. As for the decomposition temperature, the relatively poor prediction evidenced by R^2 of 0.787, may be due to the weaker ability of embedded features in describing intermolecular interactions than the molecular structural characteristics. However, in comparison to the message passing neural network (MPNN) without embedded features, which has an MAE value of 39 °C, the smaller MAE suggests that our model achieves better prediction accuracy.[40,41] In a word, considering the potential impact of dataset differences on the model's prediction results, our model shows satisfactory performance in terms of accuracy, effectiveness, and comprehensiveness compared to previous work, as is shown in Table 1.

After training the model, the properties including density, D_v, P and T_d of the 2698 generated molecules, were predicted by the model (see the ESI data†) and screened through various criteria. The step-by-step screening can be visualized using colour-mapped three dimensional (3D) scatter plots in Fig. 6. As shown in the top left panel, the predicted properties of the 2698 molecules conform to some known common rules of energetic materials, such as a linear correlation between density and D_v/P, and a negative correlation between density and decomposition

Table 1 Compared with models in previous literature

Property		Our models	Song[29]	Elton[30]	Casey[42]	Hou[43]	Huang[44]	Yang[45]
Electronic structure calculation		**Yes**	No	No	Yes	No	Yes	Yes
Density (g cm^{-3})	Samples	**>900**	>1000		>26 000	>400	—	
	MAE	**0.027**	0.042	0.06	0.035	0.026	—	0.040
Detonation velocity and pressure	Samples	**>900**	>500		>26 000	>400	>400	—
(km s^{-1}/GPa)	MAE	**0.20/1.58**	0.24/2.38	0.31/2.73	0.30/1.80	0.34/1.49	0.235/1.788 (RMSE)	—
Decomposition temperature (°C)	Samples	**>500**	>500	—	—	—	—	
	MAE	**21.5**	30.8	—	—	—	52.07 (RMSE)	

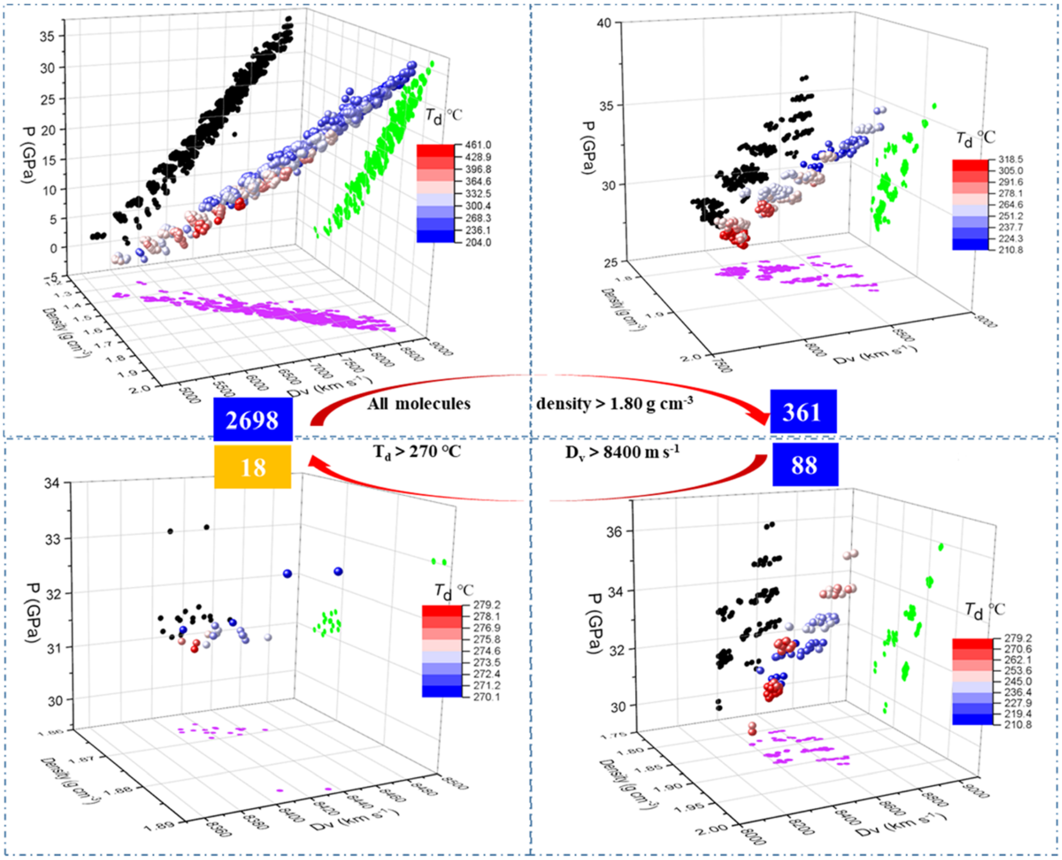

Fig. 6 3D scatter plots of molecules after different screening steps, as well as projections on various planes (green, pink, and black dots represent projections on density/D_v plane, density/P plane, and D_v/P plane, respectively).

temperature.[40] We used the density of 1,3,5-trinitro-1,3,5-triazinane, (RDX), a typical energetic material, as the first criterion for screening, and only the molecules with density greater than 1.80 g cm^{-3} were retained, decreasing the number of molecules from 2698 to 361 as indicated in the top right panel of Fig. 6. The 3D scatter plot shows that the molecules with T_d (thermal decomposition temperatures) above 270 °C (red dots) were located in areas with relatively low D_v (detonation velocities) values of 8000 m s^{-1}, whereas the molecules with D_v greater than 8800 m s^{-1} (blue dots) were mostly scattered in areas with relatively low T_d of 210 °C. Upon introducing screening criteria on energy (D_v greater than 8400 m s^{-1}) and thermal stability (T_d greater than 270 °C) successively, the number of molecules decreased from 361 to 88 (bottom right panel of Fig. 6) at first, and then further decreased to 18 (bottom left panel of Fig. 6).

On the other hand, the synthetic accessibility also plays an important role in the application of the targeted molecules. In 2009, Ertl and Schuffenhauer proposed SAscore for estimating the synthesizability of drug molecules[46] based on contributions of molecular fragments and complexity, which has been used in the field of energetic materials.[26,27] The greater synthesis

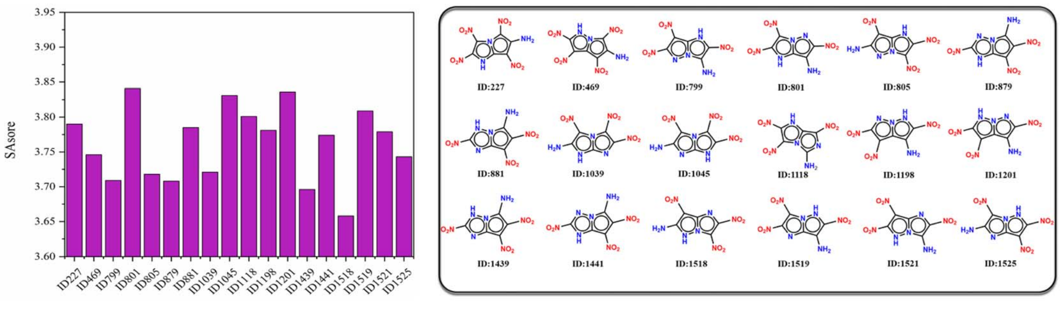

(a)

(b)

Fig. 7 (a) SAscore and (b) molecule structure of the screened molecules.

Table 2 Calculated results of density for the 10 molecules

Index	M (g mol^{-1})	V (cm^3 mol^{-1})	ν	σ_{tot}^2	ρ (g cm^{-3})
A	257.115	140.630	0.172	192.0087	1.816
B	257.111	140.659	0.176	241.136	1.841
C	257.115	139.668	0.125	521.1232	1.917
D	257.119	140.135	0.142	410.3513	1.892
E	257.119	140.517	0.178	202.3609	1.825
F	257.116	140.745	0.219	325.1201	1.886
G	257.116	140.661	0.158	393.938	1.897
H	257.116	141.156	0.140	354.151	1.856
I	257.106	139.686	0.208	239.494	1.874
J	301.121	160.692	0.179	199.691	1.865

difficulty corresponds to the larger score. Fig. 7 depicts the SAscore and structures of the 18 screened molecules. Most of the candidate molecules that are easy to synthesize are found to be 3*N*-substituted molecules. Next, the top 10 molecules (ID number: 1518, 1439, 879, 799, 805, 1039, 1525, 469, 1441 and 1521) with lowest SAscore, were taken for DFT simulation to further evaluate their overall performance, as well as prediction accuracy of the D-MPNN model.

Model evaluation

In this study, we utilized DFT to evaluate the fundamental properties of selected fused [5,5] bicyclic heterocycle energetic materials. We ensure that all optimized structures exhibit local energy minima on the potential energy surface with no imaginary frequencies before performing calculations. For clarity the molecules with the 10 lowest SAscores (ID805, ID799, ID1039, ID1518, ID1525, ID879, ID1439, ID1521, ID1441, ID469) were represented by letter A to J following ascending order, and the ID number alongside the structures of the 10 molecules is show in Table S7 of ESI.†

Density

We used the equation proposed by Politzer *et al.*[47] to calculate the density of the selected 10 fused [5,5] biheterocyclic energetic materials. Table 2 shows the calculated results of molecular mass, volumes and related data after all of the structures were optimized (more detail is referred to the ESI†).

As shown in Table 2, the densities of the 10 fused [5,5] biheterocyclic molecules are within the ranges of 1.816 g cm^{-3} to 1.917 g cm^{-3}. Except for molecule J ($C_6H_3O_8N_7$), the remaining molecules share the same molecular formula ($C_5H_3O_6N_7$) and similar structure, which results in the close values of M and V. On the other hand, the scattered values of ν (the balance between positive and negative electrostatic potentials) and σ_{tot}^2 (the total mean square error of the electrostatic potential), could be responsible for the differences in density. Among the 10 molecules, G and D were found to possess relatively high density.

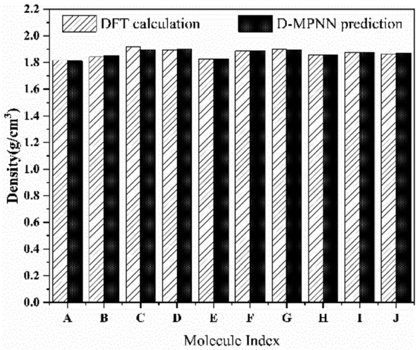

Fig. 8 Comparison between the predicted and calculated results of density for the 10 molecules.

We further evaluated the accuracy of the D-MPNN model by comparing the predicted results with those obtained from rigorous DFT calculation. As shown in Fig. 8, the density predicted by the D-MPNN embedded with features closely approximates that predicted by the DFT method. The largest relative deviation, occurring at molecule C, is 0.01 g cm^{-3}, and the average deviation is 0.006 g cm^{-3}. Moreover, the ordering of results from DFT calculations is consistent with the model, which demonstrates the high prediction model accuracy of the D-MPNN model embedded with additional features.

Heat of formation

We calculated heat of formation (HOF) of the 10 selected molecules based on the designed isodesmic reactions (Table S5 in ESI†). The calculated results are shown in Table 3.

The HOFs of the ten molecules are within the ranges of 271.314 kJ mol^{-1} to 424.924 kJ mol^{-1}. As energetic materials, their high positive HOF means higher energy contained, which

Table 3 The calculated results of E_0 (total energy), ZPE (zero-point energy), and HOF of the 10 molecules

Index	E_0 (a.u.)	ZPE (kJ mol^{-1})	$\Delta H_{\text{f,gas}}$ (kJ mol^{-1})	ΔH_{sub} (kJ mol^{-1})	$\Delta H_{\text{f,solid}}$ (kJ mol^{-1})
A	−1026.851	322.850	373.797	26.526	347.271
B	−1026.860	322.724	341.562	26.608	314.954
C	−1026.865	324.415	337.399	29.859	307.540
D	−1026.843	323.112	397.907	29.525	368.381
E	−1026.844	322.193	403.906	26.858	377.048
F	−1026.836	327.742	302.597	31.282	271.314
G	−1026.824	322.986	443.610	30.125	413.484
H	−1026.823	323.199	453.979	29.055	424.924
I	−1026.832	321.705	423.918	28.405	335.691
J	−1215.340	358.095	365.684	29.994	395.512

Table 4 The calculated results of Q, D_v and P of the 10 molecules

Index	Q (cal g^{-1})	D (m s^{-1})	P (GPa)
A	1482.992	8526.319	33.024
B	1452.951	8482.811	32.688
C	1146.060	8472.734	32.610
D	1502.613	8554.386	33.241
E	1501.669	8565.828	33.331
F	1412.388	8422.975	32.228
G	1544.537	8613.439	33.702
H	1555.171	8628.227	33.818
I	1527.832	8590.055	33.519
J	1569.385	8603.008	33.528

could be attributed to the introduction of nitrogen-rich heterocycles and fused skeletons.

Detonation velocity and detonation pressure

Based on the density and heat of formation calculated by DFT, their detonation heat (Q), detonation velocity (D_v), and detonation pressure (P) of the 10 candidate molecules were obtained using the semi empirical Kamlet–Jacobs formula, which has been proven to be reliable for predicting the detonation performance of high-nitrogen compounds.[48] Table 4 shows the calculated results of Q, D_v and P of the 10 molecules.

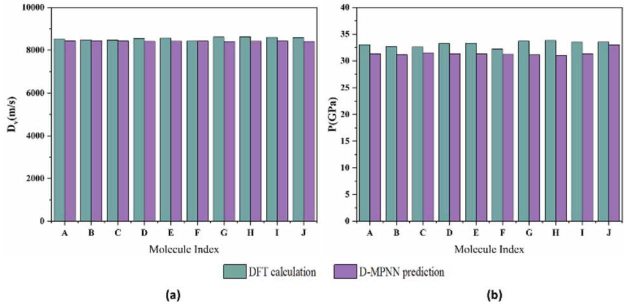

Fig. 9 Comparison between the predicted and calculated values of (a) D_v, (b) P for the 10 molecules (blackish green represents the results measured by calculated using K–J equation, whereas purple represents the results predicted by model).

The comparison between the calculated results and the values predicted by the D-MPNN model is depicted in Fig. 9. The average deviations for detonation velocity and detonation pressure is 0.018 km s^{-1} and 1.202 GPa, respectively, indicating a high level of agreement.

Thermal stability analysis

In this section, we used bond dissociation energy (BDE), HOMO–LUMO energy gap, electrostatic surface potential (ESP) to evaluate the thermal stability of the 10 promising candidates.

Bond dissociation energy

The smallest Mayer bond order for all molecules is C–NO_2, so we only consider BDE after nitro group dissociation. The calculated results are shown in Table 5. The values of all the molecules are greater than 120 kJ mol^{-1}, meeting the stability criteria for high energy density materials,[49] and regional distribution of molecular electrostatic potential in Fig. S4 (ESI)† also provides additional evidence for the stability of concerning molecule. Molecule F and molecule G have high BDE value, implying relatively high stability.

HOMO–LUMO energy gap

HOMO represents the ability of to give electrons, while LOMO represents the ability to receive electrons, hence the HOMO–LUMO energy gap is related to the electronic transition from HOMO to LUMO. A high HOMO–LUMO gap means low sensitivity to external stimuli.[50] The HOMO–LUMO diagram and energy gap values of the candidate molecules are shown in Fig. 10 and Table 6, respectively.

Electrostatic surface potential

The ESP of the 10 molecules is shown in Fig. 11, where the red and blue regions represent the positive and negative charge areas,[51] are mainly locating in the electron-withdrawing part (nitro group) or the electron-donating part (amino group). The integral area of the negative region exceeds that of the positive region, indicating that all ten compounds exhibit low mechanical sensitivity (Fig S3 in ESI†). Molecule F and molecule G demonstrate higher stability, as lower ESP values correspond

Table 5 The calculated results of BDE[a]

Index	E^a (kJ mol^{-1})	E^b (kJ mol^{-1})	E (NO_2) (kJ mol^{-1})	BDE (kJ mol^{-1})
A	−1026.852	−821.619	−205.133	261.224
B	−1026.860	−821.629	−205.133	257.895
C	−1026.865	−821.632	−205.133	261.214
D	−1026.843	−821.612	−205.133	255.372
E	−1026.844	−821.611	−205.133	264.081
F	−1026.880	−821.630	−205.133	308.446
G	−1026.824	−821.591	−205.133	264.916
H	−1026.824	−821.592	−205.133	260.526
I	−1026.832	−821.601	−205.133	257.396
J	−1215.340	−1010.111	−205.133	253.172

[a] (E_a and E_b represent the total energy of molecule before and after dissociation, respectively).

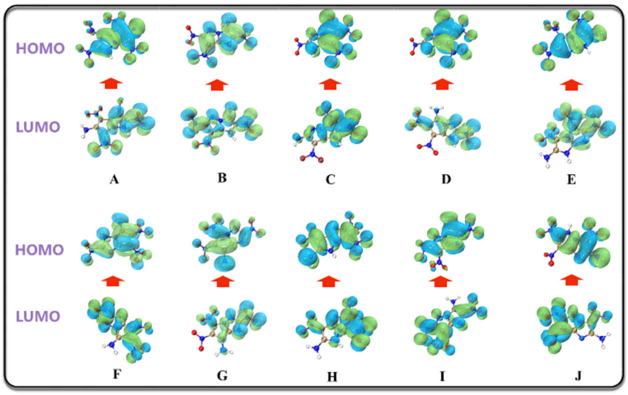

Fig. 10 HOMO–LUMO diagram of the 10 molecules.

Table 6 Molecular orbital values of the 10 molecules[a]

Index	HOMO (ev)	LUMO (ev)	GAP (ev)
A	−7.011	−4.148	2.863
B	−7.130	−3.914	3.216
C	−7.487	−4.167	3.320
D	−7.305	−3.541	3.763
E	−7.150	−4.072	3.078
F	−7.399	−2.983	4.417
G	−7.159	−3.309	3.850
H	−7.027	−4.099	2.927
I	−6.717	−3.944	2.773
J	−6.992	−4.472	2.520

[a] From the calculation results, F and G also show superior stability among the 10 molecules.

to stronger stability.[52,53] The calculated results are consistent with those of BDE and HOM–LUMO energy gap. Among the two notable molecules with high and comparable stability, molecule G exhibits better detonation performance than F, making it a suitable candidate for of fused [5,5] biheterocyclic energetic material.

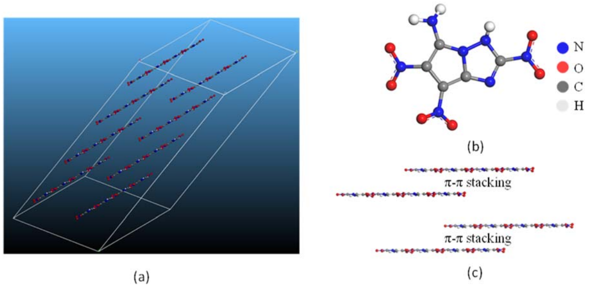

Fig. 12 (a) The crystal structure, (b) planar molecular structure and (c) three-dimensional (3D) structure based on π–π stacking of molecule G.

Crystal prediction and intermolecular interaction

Crystal structure. For molecule G, Dreiding force field was adopted to predict the crystal structure,[47] and the result is shown in Fig. 12(a). The predicted space group and cell parameters are listed in Table 7. Since the stable polycrystalline form usually shows lower total energy, molecule G is inferred to the $P\bar{1}$ space group, of which the total energy is the lowest among the structures under discussion. Moreover, the corresponding density for $P\bar{1}$ space group agrees well with the predicted value of molecule G in Table 7, further confirming the conjecture. As shown in Fig. 12(c), molecule G present a layered π–π stacking structure with face-to-face type, which could offset the shortening of the interlayer distance, increase interlayer attraction, and makes the crystal packaging compact. Thereby the generation of hot spots is prevented through interlayer sliding when subject to external stimuli,[54] accounting for the superior stability of molecule G.

Intermolecular interaction analysis. In order to further understand the stability and sensitivity of molecule G, the two-dimensional (2D) fingerprint based on Hirshfeld surface was analysed on detailed intermolecular interaction.[55,56] The Hirshfeld surface is shown in Fig. 13(a), where red and blue regions respectively represent strong and weak intermolecular interactions, respectively. As can be found, the red area only

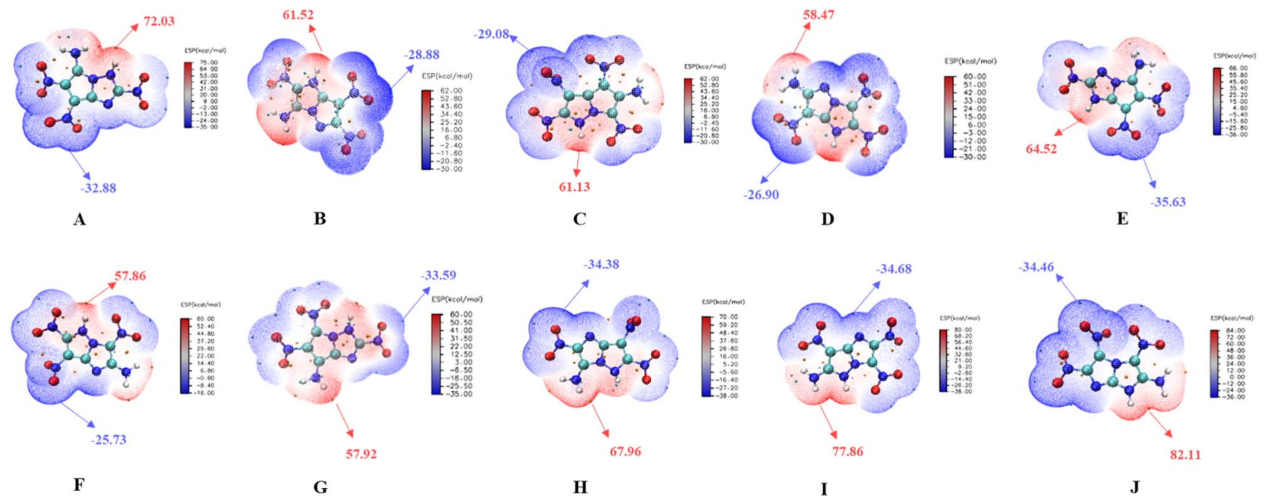

Fig. 11 The maximal and minimal ESP values (kcal mol^{-1}) of the 10 molecules.

Table 7 Parameters calculated by Dreiding force field

SG	E_{total} (kJ mol^{-1})	a (Å)	b (Å)	c (Å)	α (°)	β (°)	γ (°)	ρ (g cm^{-3})
$P\bar{1}$	58.859	11.314	7.812	8.178	134.667	71.509	87.218	1.898
$P2_1/c$	59.237	11.512	5.210	15.107	90.000	69.364	90.000	2.014
$C2/C$	59.621	14.766	5.247	28.167	90.000	53.102	90.000	1.957
$PBCA$	60.516	11.369	11.369	19.611	90.000	90.000	90.000	1.944
$P2_12_12_1$	62.245	6.432	7.907	17.687	90.000	90.000	90.000	1.913
$PNA2_1$	62.389	18.170	7.832	6.272	90.000	90.000	90.000	1.913
Cc	62.339	6.012	14.895	5.433	90.000	113.473	90.000	1.913
$P2_1$	61.269	7.813	12.261	9.566	90.000	83.585	90.000	1.875

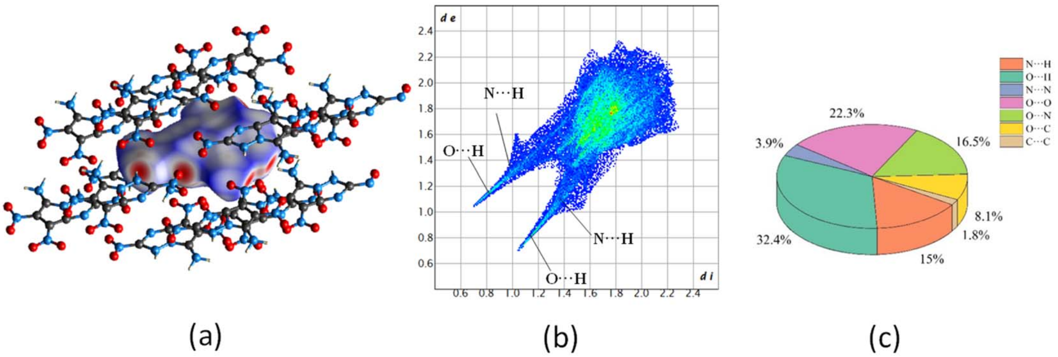

Fig. 13 (a) Hirshfeld surfaces, (b) fingerprint plots and (c) populations of close contacts of molecule G.

exists at the edge, indicating a low mechanical sensitivity. In the 2D fingerprint (Fig. 13(b)), the red area mainly locates at the edge corresponding to intermolecular hydrogen bonding interactions within the layer, with N···H interaction (15% of the total weak interactions) and the O···H interaction (32.4% of the total weak interactions) accounting for the main portion, see Fig. 13(c). Obviously, these relatively strong hydrogen bonds (total 47.4%) are the key driving force that connect molecules to one-dimensional molecular lines and then to molecular planes. In addition, significant N···O interactions (16.5%) are also observed, indicating strong π–π stacking interaction between layers of molecules.[57]

Conclusions

In this work, a high accuracy deep learning model based on D-MPNN embedded with features was established. This model assisted with high-throughput molecular screening was also applied to efficiently explore fused [5,5]-bicyclic heterocycle energetic materials. We rapidly targeted ten promising candidates from 2698 molecular structures. Further DFT calculations demonstrate that 2,6,7-trinitro-3*H*-pyrrolo[1,2-*b*][1,2,4]triazo-5-amine exhibited excellent comprehensive performance regarding both detonation properties and thermal stability, which attributes to high value of BDE and HOMO–LUMO energy gap value, low maximal ESP and unique face-to-face crystal structure. This work indicates that the combination of deep learning model embedded with features and high-throughput molecular screening, is a powerful tool for aiding rational design of novel energetic materials.

Data availability

The data supporting the findings of this study are available within the article and its ESI files.† Additional data that support the findings of this study are available from the corresponding author upon reasonable request.

Conflicts of interest

There are no conflicts to declare.

Acknowledgements

This work is supported by the National Natural Science Foundation of China (No. 22375190).

References

1 T. M. Klapötke, C. Petermayer, D. G. Piercey and J. Stierstorfer, *J. Am. Chem. Soc.*, 2012, **134**, 20827–20836.
2 B. Wang, X. Qi, W. Zhang, K. Wang, W. Li and Q. Zhang, *J. Mater. Chem. A*, 2017, **5**, 20867–20873.
3 D. Fischer, J. L. Gottfried, T. M. Klapötke, K. Karaghiosoff, J. Stierstorfer and T. G. Witkowski, *Angew. Chem. Int. Ed.*, 2016, **55**, 16132–16135.
4 D. E. Chavez, M. A. Hiskey and R. D. Gilardi, *Angew. Chem. Int. Ed.*, 2000, **39**, 1791–1793.
5 J. Zhang and J. M. Shreeve, *J. Am. Chem. Soc.*, 2014, **136**, 4437–4445.

6 Y. Cao, Z. Cai, J. Shi, Q. Zhang, Y. Liu and W. Zhang, *Energ. Mater. Front.*, 2022, **3**, 26–31.
7 J. Cai, C. Xie, J. Xiong, J. Zhang, P. Yin and S. Pang, *Chem. Eng. J.*, 2022, **433**, 134480.
8 Y. Tang, C. He, G. H. Imler, D. A. Parrish and J. M. Shreeve, *Chem. Commun.*, 2018, **54**, 10566–10569.
9 L. Hu, C. He, G. Zhao, G. H. Imler, D. A. Parrish and J. M. Shreeve, *ACS Appl. Energy Mater.*, 2020, **3**, 5510–5516.
10 P. Yin, J. Zhang, L. A. Mitchell, D. A. Parrish and J. M. Shreeve, *Angew. Chem. Int. Ed.*, 2016, **55**, 12895–12897.
11 Q. Wang, Y. Shao and M. Lu, *Chem. Commun.*, 2019, **55**, 6062–6065.
12 Z. Yang, H. Li, X. Zhou, C. Zhang, H. Huang, J. Li and F. Nie, *Cryst. Growth Des.*, 2012, **12**, 5155–5158.
13 S. A. Shevelev, I. L. Dalinger, T. K. Shkineva, B. I. Ugrak, V. I. Gulevskaya and M. I. Kanishchev, *Russ. Chem. Bull.*, 1993, **42**, 1063–1068.
14 C. He, J. Zhang, D. A. Parrish and J. M. Shreeve, *J. Mater. Chem. A*, 2013, **1**, 2863.
15 T. M. Klapötke, P. C. Schmid, S. Schnell and J. Stierstorfer, *Chem.–Eur. J.*, 2015, **21**, 9219–9228.
16 Y. Tang, C. He and J. M. Shreeve, *J. Mater. Chem. A*, 2017, **5**, 4314–4319.
17 G. H. Gu, J. Noh, I. Kim and Y. Jung, *J. Mater. Chem. A*, 2019, **7**, 17096–17117.
18 F. Ren, L. Ward, T. Williams, K. J. Laws, C. Wolverton, J. Hattrick-Simpers and A. Mehta, *Sci. Adv.*, 2018, **4**, eaaq1566.
19 S. Lu, Q. Zhou, Y. Ouyang, Y. Guo, Q. Li and J. Wang, *Nat. Commun.*, 2018, **9**, 3405.
20 Y. Zhuo, A. Mansouri Tehrani, A. O. Oliynyk, A. C. Duke and J. Brgoch, *Nat. Commun.*, 2018, **9**, 4377.
21 R. Gómez-Bombarelli, J. Aguilera-Iparraguirre, T. D. Hirzel, D. Duvenaud, D. Maclaurin, M. A. Blood-Forsythe, H. S. Chae, M. Einzinger, D.-G. Ha, T. Wu, G. Markopoulos, S. Jeon, H. Kang, H. Miyazaki, M. Numata, S. Kim, W. Huang, S. I. Hong, M. Baldo, R. P. Adams and A. Aspuru-Guzik, *Nat. Mater.*, 2016, **15**, 1120–1127.
22 H. Sahu, F. Yang, X. Ye, J. Ma, W. Fang and H. Ma, *J. Mater. Chem. A*, 2019, **7**, 17480–17488.
23 Y. Wang, Y. Liu, S. Song, Z. Yang, X. Qi, K. Wang, Y. Liu, Q. Zhang and Y. Tian, *Nat. Commun.*, 2018, **9**, 2444.
24 S. Song, F. Chen, Y. Wang, K. Wang, M. Yan and Q. Zhang, *J. Mater. Chem. A*, 2021, **9**, 21723–21731.
25 L. Wen, B. Wang, T. Yu, W. Lai, J. Shi, M. Liu and Y. Liu, *Fuel*, 2022, **310**, 122241.
26 L. Wen, T. Yu, W. Lai, J. Shi, M. Liu, Y. Liu and B. Wang, *J. Phys. Chem. Lett.*, 2021, **12**, 11591–11597.
27 L. Wen, T. Yu, W. Lai, M. Liu, B. Wang, J. Shi and Y. Liu, *Fuel*, 2022, **324**, 124591.
28 Z.-J. Lu, Y. Hu, W.-S. Dong, W.-L. Cao, T.-W. Wang, J.-G. Zhang and Q.-Y. Yu, *J. Phys. Chem. C*, 2023, **127**, 18832–18842.
29 S. Song, Y. Wang, F. Chen, M. Yan and Q. Zhang, *Engineering*, 2022, **10**, 99–109.
30 D. C. Elton, Z. Boukouvalas, M. S. Butrico, M. D. Fuge and P. W. Chung, *Sci. Rep.*, 2018, **8**, 9059.
31 K. Yang, K. Swanson, W. Jin, C. Coley, P. Eiden, H. Gao, A. Guzman-Perez, T. Hopper, B. Kelley, M. Mathea, A. Palmer, V. Settels, T. Jaakkola, K. Jensen and R. Barzilay, *J. Chem. Inf. Model.*, 2019, **59**, 3370–3388.
32 J. Gilmer, S. S. Schoenholz, P. F. Riley, O. Vinyals and G. E. Dahl, *Proceedings of the 34th International Conference on Machine Learning*, 2017, vol. 70, pp. 1263–1272.
33 P. Nguyen, D. Loveland, J. T. Kim, P. Karande, A. M. Hiszpanski and T. Y.-J. Han, *J. Chem. Inf. Model.*, 2021, **61**, 2147–2158.
34 L. H. Hall and C. T. Story, *J. Chem. Inf. Comput. Sci.*, 1996, **36**, 1004–1014.
35 L. H. Hall and L. B. Kier, *J. Chem. Inf. Comput. Sci.*, 1995, **35**, 1039–1045.
36 M. J. Frisch, G. W. Trucks, H. B. Schlegel, G. E. Scuseria, M. A. Robb, J. R. Cheeseman, G. Scalmani, V. Barone, G. A. Petersson and D. J. Fox, *Gaussian 16, Revision A.03*, Gaussian, Inc., Wallingford CT, 2016.
37 T. Lu and F. Chen, *J. Comput. Chem.*, 2012, **33**, 580–592.
38 G. Landrum, RDKit: Open-source cheminformatics, 2016. http://www.rdkit.org.
39 B. Shahriari, K. Swersky, Z. Wang, R. P. Adams and N. de Freitas, *Proc. IEEE*, 2016, **104**, 148–175.
40 C. Wespiser and D. Mathieu, *Propellants, Explos. Pyrotech.*, 2023, **48**, e202200264.
41 J. B. Choi, P. C. H. Nguyen, O. Sen, H. S. Udaykumar and S. Baek, *Propellants, Explos. Pyrotech.*, 2023, **48**, e202200276.
42 A. D. Casey, S. F. Son, I. Bilionis and B. C. Barnes, *J. Chem. Inf. Model.*, 2020, **60**, 4457–4473.
43 F. Hou, Y. Ma, Z. Hu, S. Ding, H. Fu, L. Wang, X. Zhang and G. Li, *Adv. Theory Simul.*, 2021, **4**, 6.
44 X. Huang, C. Li, K. Tan, Y. Wen, F. Guo, M. Li, Y. Huang, C. Q. Sun, M. Gozin and L. Zhang, *iScience*, 2021, **24**, 102240.
45 C. Yang, J. Chen, R. Wang, M. Zhang, C. Zhang and J. Liu, *J. Chem. Inf. Model.*, 2021, **61**, 2582–2593.
46 H.-R. Wang, C. Zhang, B.-C. Hu and X.-H. Ju, *J. Mol. Model.*, 2021, **27**, 100.
47 P. Politzer, J. Martinez, J. S. Murray, M. C. Concha and A. Toro-Labbé, *Mol. Phys.*, 2009, **107**, 2095–2101.
48 M. J. Kamlet and S. J. Jacobs, *J. Chem. Phys.*, 1968, **48**, 23–35.
49 N. Chandrasekaran, C. Oommen, V. R. S. Kumar, A. N. Lukin, V. S. Abrukov and D. A. Anufrieva, *Propellants, Explos. Pyrotech.*, 2019, **44**, 579–587.
50 C. Zhi, X. Cheng and F. Zhao, *Propellants, Explos. Pyrotech.*, 2010, **35**, 555–560.
51 V. Thottempudi, H. Gao and J. M. Shreeve, *J. Am. Chem. Soc.*, 2011, **133**, 6464–6471.
52 H. Roohi and S. Khyrkhah, *J. Mol. Model.*, 2015, **21**, 1.
53 M. R. Manaa, L. E. Fried and E. J. Reed, *J. Comput. Aided Mater. Des.*, 2003, **10**, 75–97.
54 Y. Ma, A. Zhang, C. Zhang, D. Jiang, Y. Zhu and C. Zhang, *Cryst. Growth Des.*, 2014, **14**, 4703–4713.
55 M. A. Spackman and J. J. McKinnon, *CrystEngComm*, 2002, **4**, 378–392.
56 M. A. Spackman and D. Jayatilaka, *CrystEngComm*, 2009, **11**, 19–32.
57 W. Hu, G. Zhang, P. Yang, H. Yang and G. Cheng, *Chem. Eng. J.*, 2023, **451**, 138640.